Advanced Materials Interfaces

www.advmatinterfaces.de

RESEARCH ARTICLE OPEN ACCESS

Tin Oxide-Anchored MXene Composites for Enhanced Hydrogen Evolution in Alkaline Media

Pratik Shinde[1] | Kassa Belay Ibrahim[1] | Tofik Ahmed Shifa[1] | Alessandro Gradone[2] | Pankaj Kumar[3] | Giriyapura Prabhukumara Darshan[4] | Paolo Moras[5] | Elisa Moretti[1] | Alberto Vomiero[1,3]

[1]Department of Molecular Sciences and Nanosystems, Ca' Foscari University of Venice, Venezia, Italy | [2]Institute For Microelectronics and Microsystems (IMM)-CNR Section of Bologna, Bologna, Italy | [3]Department of Engineering Sciences and Mathematics, Luleå University of Technology, Luleå, Sweden | [4]Department of Physics, Faculty of Natural Sciences, Ramaiah Technology Campus, M. S. Ramaiah University of Applied Sciences, Bengaluru, India | [5]CNR-Istituto Di Struttura della Materia (CNR-ISM), Trieste, Italy

Correspondence: Kassa Belay Ibrahim (kassabelay.ibrahim@unive.it) | Elisa Moretti (elisa.moretti@unive.it) | Alberto Vomiero (alberto.vomiero@ltu.se)

Received: 14 October 2025 | **Revised:** 21 January 2026 | **Accepted:** 13 February 2026

Keywords: electrocatalysts | hydrogen | MXene | overpotential | stability | water splitting

ABSTRACT

Efficient hydrogen generation via water splitting has long been limited by substantial energy losses; however, advances in the engineering of high-performance electrocatalysts have helped to overcome this challenge. In recent years, constructing composite structures through the deliberate optimization of two complementary materials has emerged as an effective strategy for enhancing electrocatalytic activity. Guided by this approach, we developed a SnO_2/MXene electrocatalyst for the hydrogen evolution reaction (HER) using a facile in situ hydrothermal synthesis. The resulting SnMX40 composite exhibits a low overpotential of 72 mV at a current density of 10 mA cm^{-2} and a small Tafel slope of 99 mV dec^{-1} in alkaline media, outperforming pristine SnO_2 and MXene catalysts. Furthermore, the SnMX40 catalyst demonstrates excellent durability, maintaining stable performance for up to 64 h while preserving its structural integrity, as confirmed by X-ray diffraction (XRD) and transmission electron microscopy (TEM). The enhanced HER performance is attributed to the abundance of active sites and improved electrical conductivity provided by the composite architecture.

1 | Introduction

To meet the world's energy needs today, humanity is heavily dependent on fossil fuels; however, these fuels are rapidly depleting, and their harmful effects are raising concerns for the environment. The energy demands can be practically addressed by the electrochemical energy-based sources, which show great potential in this regard. Hydrogen is identified as a fuel of the future because it is clean, renewable, and possesses a high calorific value of 282 kJ/mol [1]. The splitting of water molecules into hydrogen and oxygen using an electrochemical method is considered a simple and promising way to generate hydrogen. This method produces pure hydrogen without releasing toxic compounds into the atmosphere, making it a potentially better alternative to meet energy needs without negatively impacting the environment. The most active hydrogen evolution reaction (HER) catalysts are those based on precious metals, such as platinum, due to their quick kinetics and low overpotential [2, 3]. Its scarcity and rocketing cost seriously hindered its large-scale application. This implies that it is crucial to develop inexpensive and readily available material-based catalysts that exhibit both high activity and stability.

In recent years, MAX phases, which are layered ternary ceramics with the general formula $M_{n+1}AX_n$, where M is an early transition metal, A is a group 13–16 element, and X is carbon and/or

---

nitrogen seeks attention in water splitting catalysis [4]. Owing to their unique crystal structure, they exhibit a rare combination of metallic properties (such as high electrical and thermal conductivity and machinability) and ceramic properties (including high-temperature stability, oxidation resistance, and mechanical strength). Importantly, MAX phases are the parent materials used to derive MXenes, as the A-layer can be selectively etched out to produce 2D MXene nanosheets with the formula $M_{n+1}X_nT_x$. MXenes are typically expressed as $M_{n+1}X_nT_z$, where M denotes transition metal elements (such as Ti, V, Mo, and Cr); X can stand for C or N; T_z can represent surface terminals of O,– OH, or– F; and n can be 1–3 [4, 5]. These MXenes are typically synthesized by selectively etching or extracting "A" layers (A = Si, Al, Ga, etc.) from layered MAX ($M_{n+1}AX_n$) precursors. MXenes hold great potential as catalytic applications because of their excellent hydrophilicity, high electrical conductivity, large surface areas, and tunable structures [6]. MXenes have demonstrated exceptional performance as electrocatalysts, characterized by reduced overpotentials, low Tafel slopes, and long-term stability even at high current densities [7, 8]. A growing family of layered materials consists of 2D transition metal carbides, nitrides, or carbonitrides, which are coined as MXenes. Furthermore, research on post-transition metal oxides, sulfides, and selenides is being extensively conducted to catalyze HER in both acidic and alkaline media [8, 9]. Among them, tin (Sn) is a silver-white metal widely distributed element in the Earth's crust, belonging to Group VIA of the periodic table. Its oxide shows n-type semiconducting behaviour and exhibits a bandgap of 3.6 eV [10]. This oxide can be used as a sustainable and cost-effective alternative to precious metals for water electrolysis reactions. There is some previously reported literature that showed SnO_2 exhibits good performance for HER [11–13]. Even though the properties of MXene and SnO_2 materials are interesting, their performance in catalysis applications is poorer than that of benchmark catalysts. There are several strategies employed by researchers, such as doing [14, 15], defect engineering, alloying, heterostructure, composite formation, etc., to improve their properties [12, 16–19]. The results of multiple experiments involving the development of composite or hybrid structures with well-optimized structures and concentration indicate that successful outcomes are being achieved for HER electrocatalysis. Sn and its derivatives anchored on 2D materials have attracted increasing attention, as demonstrated by earlier studies [20]. Anchoring Sn species onto 2D supports offers clear advantages, including the suppression of agglomeration, enhanced structural stability, tailored electronic interactions, and improved charge transport, which are essential for high-performance functional materials. Among various 2D platforms, MXenes stand out due to their high electrical conductivity, diverse surface terminations, and chemically active metal sites, providing abundant and tunable anchoring sites for Sn and Sn-derived species. These unique characteristics make MXenes an ideal host for stabilizing and modulating Sn at the atomic or nanoscale level. However, despite rapid progress in MXene synthesis and applications, the fundamental mechanisms governing Sn and its derivatives anchored on MXene surfaces remain largely unexplored and understudied. A systematic investigation into the anchoring behavior, interfacial chemistry, and resulting structure–property relationships is therefore highly warranted, both from fundamental and application-driven perspectives.

Here, we coupled SnO_2 and $Ti_3C_2T_x$ MXene nanosheets (denoted as SnO_2/MXene) for efficient HER performance, considering the promise of Sn-based catalysts toward the H_2 production, but its intrinsic HER activity is hindered by low electrical conductivity and the unique propertiesof 2D MXene materials (large specific surface area, good hydrophilic surfaces, tuneable termination groups, and high metallic conductivities, etc). As a result, the SnO_2/MXene composite results in activity with an overpotential of 72 mV at 10 mA/cm^2, 203 mV at 50 mA/cm^2, and a Tafel slope of 99 mV/dec in an alkaline solution. The composites offer a large number of active sites for electrocatalytic activity, and the synergistic effect between them results in higher HER performance as compared to pristine materials. In summary, we provide a straightforward and universal method for designing new catalysts that are active and stable for the HER.

2 | Experiments

2.1 | Synthesis of $Ti_3C_2T_x$ MXene

2 g of titanium aluminium carbide (Ti_3AlC_2 90%, Sigma Aldrich) MAX powder was added into a Teflon beaker containing 40 mL of hydrofluoric (HF-48%, Sigma Aldrich) acid solution. The mixture was vigorously stirred at 40°C for 72 h. The obtained product was washed multiple times with distilled water and dried at 60°C for 12 h.

2.2 | Synthesis of SnO_2/MXene Composites

The powder of 3 mmol of tin chloride dihydrate ($SnCl_2$ $2H_2O$, Sigma Aldrich) was added to 20 mL of distilled water and stirred for 30 min. In another beaker, 20 mg of as-prepared MXene was added to 15 mL of distilled water and ultrasonicated for 30 min. Then, both solutions were mixed and further stirred for 30 min. The well-mixed solution was transferred into a 50 mL Teflon-lined stainless steel autoclave and heated at 200°C for 24 h. After the autoclave cooled naturally, the precipitated composite powder was washed several times with distilled water and ethanol and dried overnight at 60°C. The prepared composite is named SnMX20. Similarly, the SnMX40 and SnMX60 composites were also prepared by adding 40 and 60 mg of MXene, respectively. The pristine SnO_2 material was prepared with the same procedure without the addition of MXene.

2.3 | Characterization of the Materials

The crystallinity and phase of materials were analyzed by X-ray diffraction (XRD) using a Philips PW1050/37 diffractometer. The chemical composition of materials is analyzed by Fourier transform infrared spectroscopy (FTIR, Nicolet 6700 FTIR Spectrometer). The morphology and structure were investigated using a field emission scanning electron microscope (FESEM, FEI Magellan 400FEG-SEM). The atomic structure of the material was studied by high-resolution transmission electron microscopy (HRTEM, FEI TECNAI F20 microscope operating at 200 keV). The instrument is also equipped with a dispersion micro-analysis of energy (EDS-energy-dispersive X-ray spectroscopy) and the

STEM accessory. STEM pictures were recorded using a high-angle annular dark field (HAADF) detector: in this imaging mode, the intensity I is proportional to $Z^{1.7}t$, where Z is the mean atomic number and t is the thickness of the specimen. X-ray photoemission spectroscopy (XPS) measurements were carried out at the VUV-Photoemission beamline of the Elettra synchrotron (Trieste, Italy) using 750 eV photon energy and an R-4000 electron spectrometer.

2.4 | Electrochemical Measurements

The ink of the catalyst was prepared by dispersing 2 mg of electrocatalyst in a mixture of 100 µL isopropanol and 10 µL of 5 wt.% Nafion solution, followed by 1 h of ultrasonication in a water bath. Then, homogenously mixed ink was used to prepare the working electrode by drop-casting it on a 1 × 1 cm^2 area of Nickel foam and dried in the oven before electrochemical measurements. The platinum wire and Ag/AgCl electrode were used as a counter and reference electrode, respectively. All potentials were referenced to the RHE by the Nernst equation: ERHE = E(Ag/AgCl) + 0.059 pH + EoRHE. All electrochemical tests were performed at room temperature in a 1.0 M KOH solution. The performance of the hydrogen evolution catalyst was measured using linear sweep voltammetry (LSV) beginning at 0 V and ending at −2.0 V vs. RHE with a scan rate of 10 mV/s. Electrochemical impedance spectroscopy (EIS) analysis was conducted in the same setup in the frequency range of 0.1 Hz to 100 kHz at a modulation amplitude of 10 mV. Electrochemically active surface area (ECSA) was evaluated by cyclic voltammetry (CV) cycling from −0.1 to −0.3 V versus Ag/AgCl at scan rates of 120 to 200 mV/s. The stability performance of the SnMX40 electrocatalyst was tested using the chronopotentiometry technique at current densities of 10, 50, and 100 mA/cm^2. The three-electrode cell configuration is used to perform electrochemical characterisations connected to a potentiostat (Biologic, SP-300).

3 | Results and Discussion

The synthetic procedures of MXene and SnO_2/MXene composites are schematically shown in Figure 1a. First, Al element layers from the bulk Ti_3AlC_2 MAX phase were selectively etched with HF acid, which develops accordion-like $Ti_3C_2T_x$ MXene structures. Then, this MXene structure with numerous terminating functional groups, such as —O, —OH, or —F, was used to grow SnO_2 material on it. These negative terminals of MXene facilitate the nucleation and assist in growing the SnO_2 material.

The phases and crystallinity of the as-prepared samples are investigated using powder XRD analysis. The MAX phase-Ti_3AlC_2 showed strong diffraction peaks at $2\theta = 9.5°$ (002), 19.0° (004), 34.0° (100), 36.7° (103), 38.9° (104), 41.7° (105), 48.3° (107), 56.4° (107), and 60.1° (110), as shown in Figure S1 [21, 22]. The characteristic peaks MXene ($Ti_3C_2T_x$) at 2θ = 8.8°, 18.2°, 27.5°, 34.9°, and 60.8° correspond to (0 0 2), (0 0 4), (0 0 6), (0 0 8), and (1 1 0) planes, respectively (Figure S1) [23]. In MXene ($Ti_3C_2T_x$) preparation, peaks at 9.5° and 19.0° were significantly displaced to lower angles of 8.8° and 18.2°, respectively, because of the selective etching of Al layers in the MAX phase. This shift indicates that the synthesized $Ti_3C_2T_x$ MXene has a larger *d* spacing than the initial Ti_3AlC_2 MAX phase. The structural expansion resulting from etching and the significant substitution of Al with −F and −OH/= O termination groups are the causes of an increase in *d* spacing. In $Ti_3C_2T_x$ MXene, the strongest peak at $2\theta = 38.9°$ almost vanished, indicating that a significant amount of Al layers were removed from Ti_3AlC_2 [24]. Additionally, the XRD pattern of $Ti_3C_2T_x$ MXene showed less crystallinity and disordered structural order in the sheets due to the broadness and suppressed intensity of the peaks, indicating that the treatment in HF acidic solution was successful [25]. There are less intense peaks at 25° and 37° corresponding to the partially oxidized TiO_2 [26]. The XRD patterns of as-prepared SnO_2 and SnO_2/MXene composites are displayed in Figure 1b. The recorded diffraction peaks of SnO_2 at 26.6°, 33.8°, 37.9°, 51.7°, 54.7°, 61.8°, 65.9°, 71.2°, and 78.7° were indexed to (110), (101), (200), (211), (220), (310), (301), (202), and (321) planes of cassiterite SnO_2 (JCPDS No. 41–1415). XRD spectra of SnMX20, SnMX40, and SnMX60 composites show peaks of both materials, without any additional peaks. Thus, the XRD results confirm the successful synthesis of $Ti_3C_2T_x$ MXene, SnO_2, and their composites. The infrared spectra of the MXene, SnO_2, and composite materials were found to be quite similar, as presented in Figure S2. The broad stretching peak of vibration at approximately 1600 and 3430 cm^{-1} was ascribed to the hydroxyl group's absorption peak. The bands present below 800 cm^{-1} are attributed to the vibrational stretching modes of metal and oxygen. The spectra of all three composites show equivalent characteristic peaks to the bare materials.

The morphology and structural characteristics of the synthesized materials were investigated by field-emission scanning electron microscopy (FESEM). The unetched Ti_3AlC_2 MAX phase exhibits a densely stacked multilayer structure. After selective etching of the Al atomic layers, the resulting $Ti_3C_2T_x$ MXene displays a characteristic accordion-like morphology (Figure S3). FESEM images also reveal that SnO_2 possesses a nanoparticle-like morphology (Figure S3). As shown in Figure 1c–e, SnO_2 nanoparticles are uniformly decorated on the surface as well as intercalated between the layers of the $Ti_3C_2T_x$ MXene sheets in the composite samples.

To further elucidate the microstructure, TEM analysis was performed on the SnMX40 composite, as shown in Figure 2. The low-magnification TEM image shows a large number of nanoparticles uniformly embedded within a flake-like matrix of comparable size and morphology, attributable to the MXene component. In the higher-magnification image (Figure 2b), SnO_2 nanoparticles are clearly observed to be anchored on Ti-based 2D layers, confirming the presence of $Ti_3C_2T_x$ MXene. In addition, a large and well-defined layered structure observed on the surface of the carbonaceous matrix (highlighted by the red arrow) likely corresponds to an additional MXene layer. HRTEM images (Figure 2c) show that the nanometric particles are embedded within a partially amorphous matrix. The lattice fringes observed in both the HRTEM images and the corresponding fast Fourier transform (FFT) inset (yellow square) can be indexed to the cassiterite phase of SnO_2, which is the thermodynamically stable crystalline form under ambient conditions, in which SnO_2 crystallizes in a tetragonal rutile-type structure (space group $P4_2/mnm$). The measured interplanar spacing of 0.33 nm corresponds to the (110) plane of SnO_2. Furthermore, additional lattice spacings highlighted in red in both the HRTEM image and FFT inset are

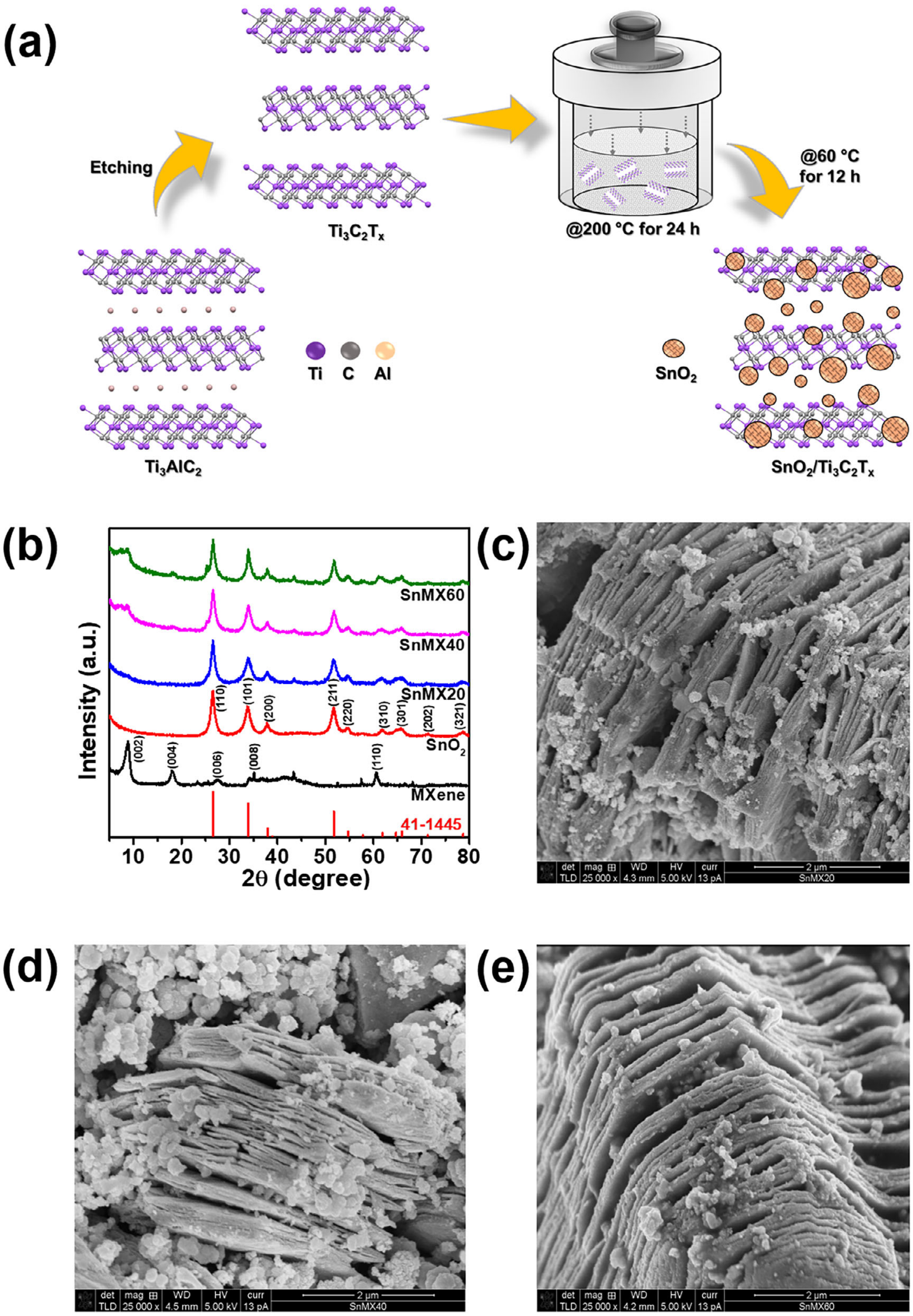

FIGURE 1 | (a) Schematic representation of the preparation method of SnO_2 and MXene composites, (b) XRD patterns of synthesised materials. FESEM images of (c) SnMX20, (d) SnMX40, and (e) SnMX60.

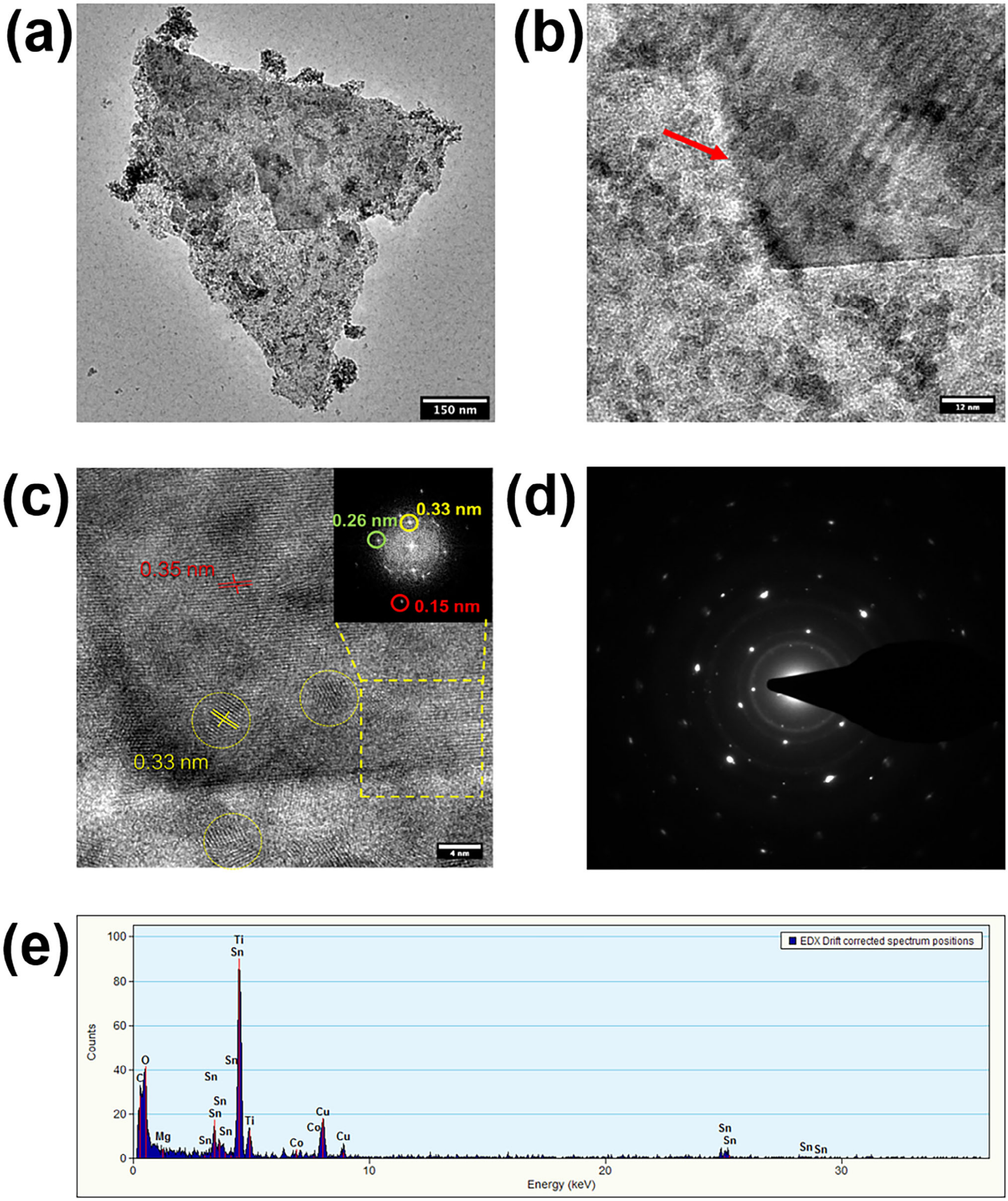

FIGURE 2 | TEM analysis of SnMX40 composite (a) Low magnification TEM micrograph, (b) High magnification TEM micrograph, (c) HR-TEM analysis. The inset shows an FFT image of a specific area (yellow square), (d) SAED image, (e) EDS spectrum of SnMX40 composite.

attributed to the MXene phase, consistent with the diffraction peaks observed in the XRD patterns.

The SAED pattern shown in Figure 2d exhibits characteristic polycrystalline diffraction rings, indicating the presence of multiple crystallites with varying sizes and orientations, in agreement with the TEM observations at higher magnification. Energy-dispersive X-ray spectroscopy (EDS) analysis of the SnMX40 composite (Figure 2e) confirms the presence of Sn, Ti, C, and O elements, verifying the coexistence of SnO_2 and MXene

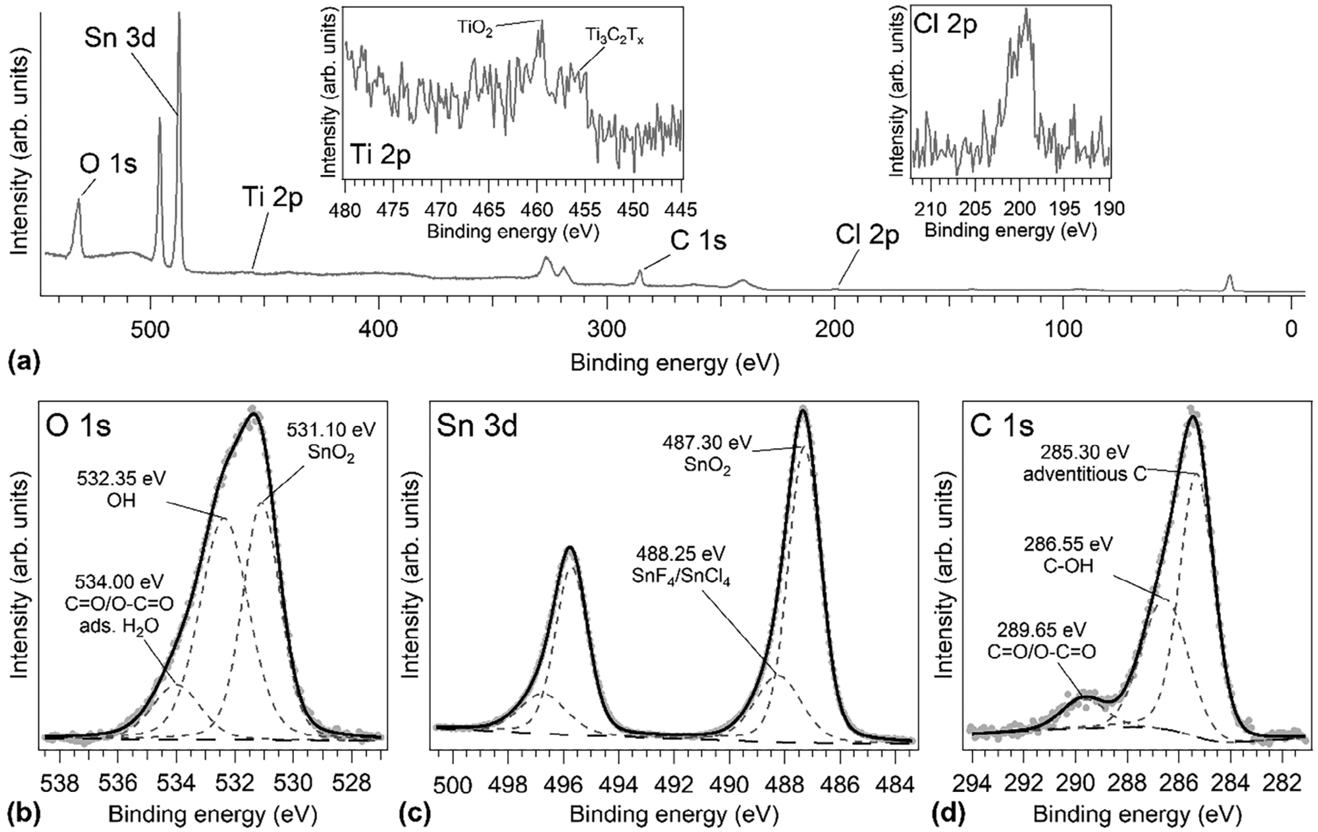

FIGURE 3 | XPS core level data of the SnMX40 composite at 750 eV photon energy: (a) survey spectrum with insets of the Ti 2p and Cl 2p regions; (b) O 1s spectrum, (c) Sn 3d spectrum, and (d) C 1s spectrum.

components, in good agreement with the HRTEM and SAED results. Furthermore, low-magnification high-angle annular dark-field scanning TEM (HAADF-STEM) images (Figure S5) provide a clearer visualization of the nanoparticle distribution within the MXene matrix. Figure S6 presents EDS point analyses based on the STEM micrographs, where spectra collected from nanoparticle-rich regions show only Sn and O signals without contributions from the low-contrast matrix. The measured Sn/O atomic ratio of approximately 0.46 closely matches the stoichiometric value of SnO_2, further confirming the cassiterite nature of the nanoparticles.

XPS analysis was performed to investigate the surface elemental composition of the SnMX40 system. The O 1s, Sn 3d, and C 1s core levels are clearly detected in the survey spectrum (Figure 3a). In contrast, the Ti 2p signal is only about 2% of the intensity of the Sn 3d levels (left inset in Figure 3a). The lineshape of the Ti 2p spectrum suggests the presence of $Ti_3C_2T_x$ (Ti $2p_{3/2}$ at about 455–456 eV) and TiO_2 (Ti $2p_{3/2}$ at about 459 eV), which are expected to form following the exfoliation of the Ti_3AlC_2 MAX phase bulk crystal by HF [27]. The very low Ti 2p signal indicates that the $Ti_3C_2T_x$ flakes are buried below the surface. The O 1s spectrum (Figure 3c) can be fitted with three peaks corresponding to O in SnO_2 (531.10 eV) [SnO_2] [28], OH groups (532.35 eV), and C═O/O─C═O plus adsorbed H_2O (534.00 eV). In Figure 3c, the fitting of the Sn 3d levels highlights the presence of two doublets with Sn $3d_{5/2}$ at 487.30 and 488.25 eV. The position of the former doublet confirms the formation of SnO_2 (cassiterite phase) [SnO_2], while the latter doublet at higher binding energy derives from Sn atoms coordinated with four halogen atoms, such as in SnF_4 (Sn $3d_{5/2}$ at 488.4 eV) [29] and $SnCl_4$ (Sn $3d_{5/2}$ at 488.0–488.3 eV) [30]. Indeed, both F and Cl are present in the SnMX40 composite: the exfoliation of Ti_3AlC_2 by HF leads to F termination of the $Ti_3C_2T_x$ flakes (together with O and OH); Cl is contained in SnCl2 · 2H2O, which is employed for the synthesis of SnO_2. The right inset in Figure 3a shows that residues of Cl are detected in the SnMX40 composite. However, the intensity of the Cl 2p core levels is too low to fully explain the intensity of the deepest Sn 3d doublet, due to $SnCl_4$. This observation leads us to think that SnF_4 is formed as a consequence of the chemical interaction between SnO_2 nanoparticles and the F terminations of the $Ti_3C_2T_x$ flakes. We speculate that this mechanism stabilizes the SnMX40 composite. As a final remark, the position of the C 1s peak corresponding to adventitious carbon at 285.30 eV demonstrates that charging effects are negligible.

The HER electrocatalytic performance of the synthesized catalysts was evaluated in a 1.0 M KOH electrolyte. The corresponding linear sweep voltammetry (LSV) curves are presented in Figure 4a. Among all the tested catalysts, SnMX40 exhibits the best HER activity, requiring an overpotential of 200 mV to achieve a current density of 50 mA cm^{-2}, which is significantly lower than those of SnMX20 (234 mV), SnMX60 (256 mV), pristine SnO_2 (285 mV), and MXene (301 mV). Notably, SnMX40 delivers overpotentials of only 72 mV at 10 mA cm^{-2} and 203 mV at 50 mA cm^{-2}, demonstrating a marked improvement over the individual SnO_2 and MXene catalysts. The superior catalytic performance of SnMX40 can be attributed to the strong interfacial

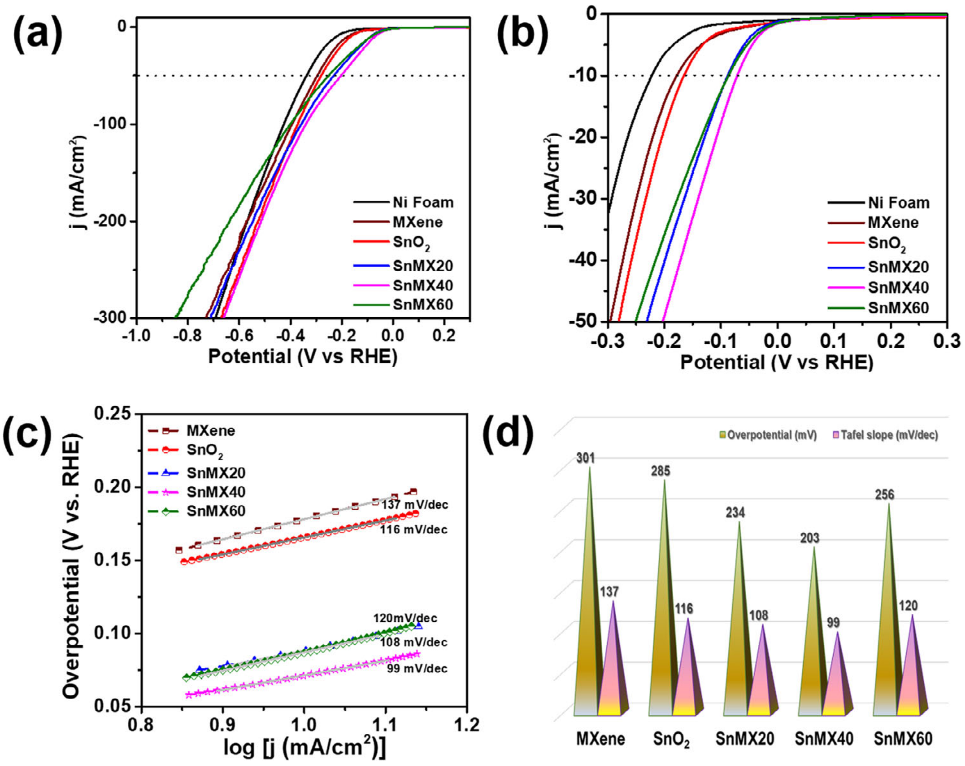

FIGURE 4 | Electrochemical performance of electrocatalysts in 1 M KOH electrolyte (a) LSV curves of prepared electrocatalysts, (b) Magnified image of LSV curves, (c) Corresponding Tafel slopes, (d) Schematic representing overpotential (at 50 mA/cm^2) and Tafel slope performance comparison of electrocatalysts.

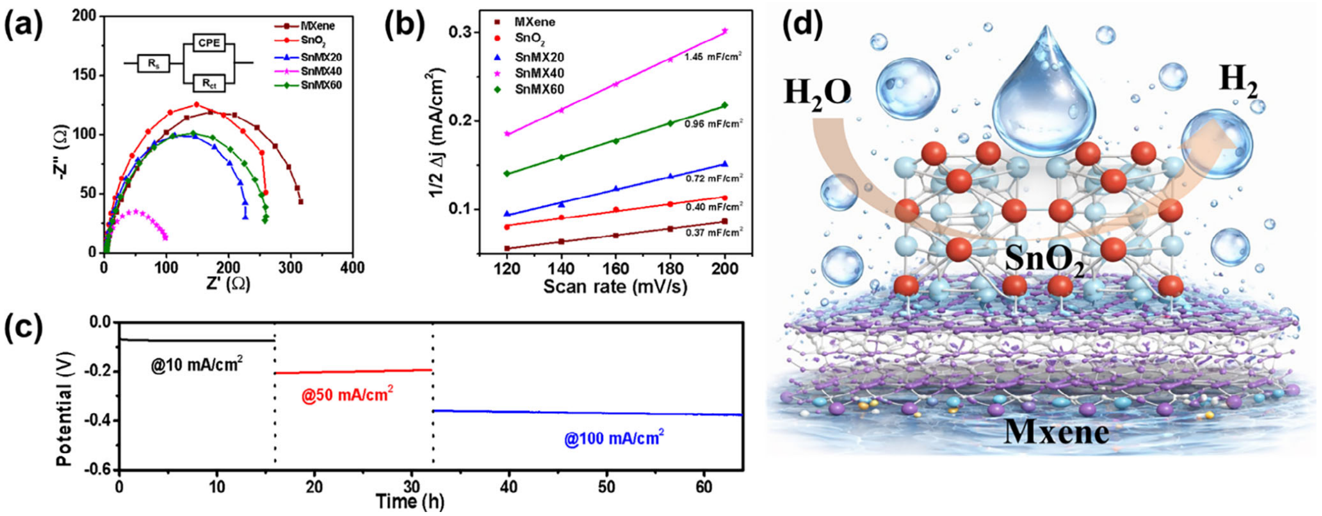

FIGURE 5 | (a) EIS curves of electrocatalysts, (b) Current vs. scan rate curves, (c) Stability test recorded for SnMX40 composite at 10, 50, and 100 mA/cm^2 current densities, (d) Schematic depicting SnO$_2$ and Mxene interface.

interaction between SnO$_2$ and MXene, the increased number of exposed active sites, and the optimized composition of the composite. To further evaluate the HER kinetics, Tafel slopes were extracted from the polarization curves (Figure 4c). SnMX40 exhibits the smallest Tafel slope of 99 mV dec^{-1}, outperforming SnMX20 (108 mV dec^{-1}), SnMX60 (120 mV dec^{-1}), SnO$_2$ (116 mV dec^{-1}), and MXene (137 mV dec^{-1}). The reduced Tafel slope in the range of 40–120 mV dec^{-1} suggests enhanced HER kinetics for SnMX40, which can be attributed to a lowered energy barrier for the Volmer step.

Based on the Tafel slope analysis, the HER on the prepared electrocatalysts in alkaline medium follows a Volmer–Heyrovsky reaction pathway which the initial Volmer step involves the electrochemical adsorption of hydrogen ($H^+ + e^- \rightarrow H$), followed by the Heyrovsky step where the adsorbed hydrogen reacts with

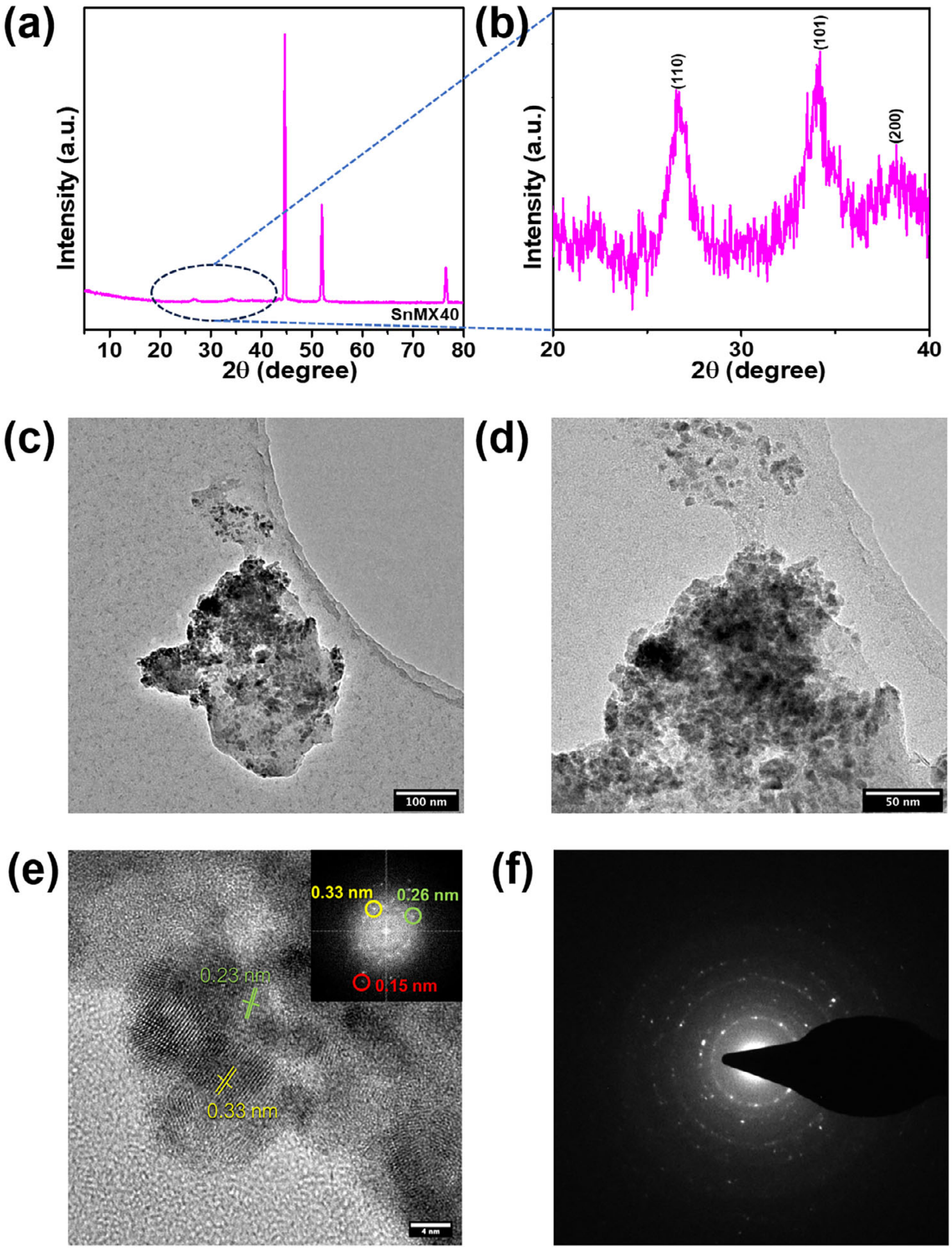

FIGURE 6 | XRD and TEM analysis of SnM40 composites after long-term stability (a) XRD pattern, (b) Magnified portion of XRD pattern, (c) Low magnification TEM micrograph, (b) High magnification TEM micrograph, (c) HR-TEM analysis of SnMX40 composite. The inset shows an FFT image, (d) SAED image.

a proton and an electron to form molecular hydrogen ($H^* + H^+ + e^- \rightarrow H_2$)*. In particular, the SnMX40 catalyst exhibits a Tafel slope of 99 mV dec^{-1}, which is close to the theoretical value expected for a Volmer–Heyrovsky mechanism, where the electrochemical desorption (Heyrovsky step) is the rate-determining step. In comparison to many of the recently reported MXene and SnO_2-based electrocatalysts, the HER activity of SnMX40 is superior (Table S1). The results reveal that a composite of SnO_2 and MXene (SnMX40) is a highly active electrocatalyst for HER in an alkaline solution with a low overpotential and quick kinetic process (Figure 4d). The superior electrocatalytic performance of SnMax40 is attributed to its provision of an optimal balance between SnO_2 active sites and MXene conductive support. Our XPS analysis provides insight into the interfacial chemical environment of the composite. The presence of a higher-binding-energy Sn 3d doublet indicates Sn atoms coordinated with halogen species, which is more reasonably attributed to Sn—F coordination arising from interfacial interactions between SnO_2 nanoparticles and F-terminated $Ti_3C_2T_x$ flakes. It should be emphasized that this Sn—F species is not proposed as an independent active phase for HER; rather, it serves as evidence of strong chemical coupling at the SnO_2/MXene interface. This contributes to improved charge-transfer efficiency and optimized adsorption–desorption energetics of hydrogen intermediates, consistent with the observed low overpotential and a Tafel slope indicative of a Volmer–Heyrovsky mechanism. At lower MXene content (SnMax20), limited conductivity and poor SnO_2 dispersion reduce activity, while excessive MXene loading (SnMax60) can block active sites and cause restacking, hindering ion access.

The performance of electrocatalysts is known to be significantly influenced by transport resistances and electrical conductivity. The EIS measurements were used to evaluate the resistance of the HER electrodes (Figure 5a). The solution resistance (R_s) is around 0.99 to 2 Ω across all electrodes; however, there is a notable difference in charge transfer resistance (R_{ct}). The R_{ct} value for the SnMX40 electrodes is ~99 Ω, which is significantly lower than the values for the SnMX20 (226 Ω), SnMX60 (256 Ω), SnO_2 (261 Ω), and MXene (317 Ω). It is commonly recognized that R_{ct} strongly correlates with the HER's kinetics, with a low R_{ct} value reflecting a higher electrode's electrocatalytic activity. The SnMX40 electrocatalyst has a high electrical conductivity and a faster charge transfer rate than other prepared catalysts. The number of active sites for HER is directly correlated with the catalyst's ECSA, which is often measured by the double-layer capacitance (C_{dl}) since it is assumed to be linearly proportional to the C_{dl} of the catalyst. The pristine MXene and SnO_2 catalysts show C_{dl} values of 0.37 and 0.40 mF/cm^2, respectively (Figure 5b). The C_{dl} of SnMX20, SnMX40, and SnMX60 composite is 0.72, 1.45, and 0.96 mF/cm^2, respectively. Therefore, among prepared catalysts, the SnMX40 catalyst exhibits the highest active sites for the HER reaction. The results are consistent with LSV plots.

In practical applications, the durability of the electrocatalyst is also a crucial parameter. The long-term cycling performance of SnMX40 was measured at the current densities of 10, 50, and 100 mA/cm^2, as shown in Figure 5c. The results indicate that the electrocatalyst is showing stable performance in alkaline media for 64 h. This could be attributed to the fact that the interfacial bonding can induce local electronic redistribution, enhance interfacial adhesion, and stabilize the heterostructure under electrochemical operation (Figure 5d).

The XRD graph recorded after the long-term HER stability test is shown in Figure 6a,b. It shows diffraction peaks of SnO_2 at 26.6°, 33.8°, and 37.9°, corresponding to the (110), (101), and (200) planes of SnO_2 nanoparticles. Furthermore, TEM analysis was carried out to check the structural stability of the SnMX40 composite after long-term stability. TEM micrographs in Figure 6c,d show nanoparticles present in a flake-like structure of MXene. The d-spacings of 0.33 nm in the high-resolution image and the FFT image in Figure 6e belong to the cassiterite phase SnO_2 material. SAED patterns showed that, even after long stability material exhibits a polycrystalline structure (Figure 6f). The low-resolution STEM-HAADF image in Figure S8 also reveals the presence of the matrix and nanoparticles. These comprehensive characterizations of the SnMX40 electrocatalyst after stability tests confirm that it is suitable for use as an electrode in alkaline water electrolysis.

4 | Summary

Therefore, in this study, we have synthesised, characterized, and systematically studied the electrochemical HER performance of SnO_2 and MXene composite. The SnMX40 catalyst requires a low overpotential of only 72 mV to reach 10 mA/cm^2, exhibits a low Tafel slope of 99 mV/dec, and exhibits long-term stability. The after-stability XRD and TEM characterizations showed stable behaviour and retained their pre-stability features after 64 h. As a result of the combined action of these two different materials, a synergistic effect is generated, which improves the charge transfer mechanism and reduces overpotential. The composites are rich in electrocatalytically active sites, which also increases HER performance over pristine materials. This work presents the importance of designing and manufacturing 2D MXene-based composite electrocatalysts for water electrolysis that are cost-effective as well as highly efficient.

Acknowledgements

This work was funded by the Kempe Foundation, the Knut och Alice Wallenberg Foundation (grant number KAW 2016.346), the ÅFORSK Foundation, and by the Europa Union project with CUP: H73C25000960006 – Codice progetto: SAFE-FA-2025-844-T2P. AV and EM acknowledge partial funding from the project COD. P2022RL4TR, CUP: H53D23009150001-funded by Bando PRIN 2022 PNRR—D.D. n. 1409 del 14/09/2022. We also acknowledge Ca' Foscari University of Venice for the SPIN2019 project. TA would like to acknowledge the Ministero dell'Università e della Ricerca (MUR) under the PRIN 2022 programme (Progetti di Ricerca di Rilevante Interesse Nazionale), Project code: H53D2300384000. Finally, we acknowledge Elettra Sincrotrone Trieste for providing access to its synchrotron radiation facilities and for financial support under the SUI internal project (proposal nr. 20235464). The PM acknowledges partial funding through the project EUROFEL-ROADMAP ESFRI of the Italian Ministry of Education, University, and Research.

Open access publishing facilitated by Universita Ca' Foscari, as part of the Wiley - CRUI-CARE agreement.

Conflicts of Interest

The authors declare no conflicts of interest.

Data Availability Statement

The data that support the findings of this study are available from the corresponding author upon reasonable request.

References

1. M. Asim, S. Zhang, Y. Wang, et al., "Self-Supporting Nicop for Hydrogen Generation via Hydrolysis of Ammonia Borane," *Fuel* 318 (2022): 123544, https://doi.org/10.1016/j.fuel.2022.123544.

2. A. Mondal and A. Vomiero, "2D Transition Metal Dichalcogenides-Based Electrocatalysts for Hydrogen Evolution Reaction," *Advanced Functional Materials* 32 (2022): 2208994, https://doi.org/10.1002/adfm.202208994.

3. P. D. Sanadi, R. K. Chougale, D. B. Malavekar, et al., "Efficient Hydrogen Evolution via Neutral Water Electrolysis Using Nanocrystalline TiO_2 Electrocatalyst," *Scientific Reports* 15 (2025): 16074, https://doi.org/10.1038/s41598-025-93371-0.

4. K. Belay Ibrahim, T. Ahmed Shifa, S. Zorzi, M. Getaye Sendeku, E. Moretti, and A. Vomiero, "Emerging 2D Materials beyond Mxenes and Tmds: Transition Metal Carbo-Chalcogenides," *Progress in Materials Science* 144 (2024): 101287, https://doi.org/10.1016/j.pmatsci.2024.101287.

5. Y. Liu, H. Xiao, and W. A. Goddard III, "Schottky-Barrier-Free Contacts With Two-Dimensional Semiconductors by Surface-Engineered Mxenes," *Journal of the American chemical society* 138 (2016): 15853–15856, https://doi.org/10.1021/jacs.6b10834.

6. X. Hui, X. Ge, R. Zhao, Z. Li, and L. Yin, "Interface Chemistry on MXene-Based Materials for Enhanced Energy Storage and Conversion

Performance," *Advanced Functional Materials* 30 (2020): 2005190, https://doi.org/10.1002/adfm.202005190.

7. L. Xiao, Q. Yang, X. Zhu, Y. Wei, and J. Wang, "Synergetic Effect and Phase Engineering by Formation of $Ti_3C_2T_x$ Modified 2 h/1T-$MoSe_2$ Composites for Enhanced Her," *Materials* 16 (2023): 6991, https://doi.org/10.3390/ma16216991.

8. J. Wu, R. Zhao, H. Xiang, et al., "Exposing Highly Active (100) Facet on a SnS_2/SnO_2 Electrocatalyst to Boost Efficient Hydrogen Evolution," *Applied Catalysis B: Environmental* 292 (2021): 120200, https://doi.org/10.1016/j.apcatb.2021.120200.

9. Z. B. Ndala, N. P. Shumbula, S. Nkabinde, et al., "Electrocatalytic Activity of Pristine and Electrochemically Activated $SnSe_2$ Nanoplates for the Hydrogen Evolution Reaction," *Journal of Electroanalytical Chemistry* 918 (2022): 116464, https://doi.org/10.1016/j.jelechem.2022.116464.

10. Y. Kong, Y. Li, X. Cui, et al., "SnO_2 Nanostructured Materials Used as Gas Sensors for the Detection of Hazardous and Flammable Gases: A Review," *Nano Materials Science* 4 (2022): 339–350, https://doi.org/10.1016/j.nanoms.2021.05.006.

11. S. Aslam, B. Ali, M. Mirza, R. Naz, W. Abbas, and M. Safdar, "Construction of SnO_2@ CrS_2 Nanocuboids via Solvothermal Synthesis for Photoelectrochemical Oer/Her Performance in Alkaline and Acidic Media and Water Detoxification Behavior," *Catalysis Letters* 154 (2024): 6333–6350, https://doi.org/10.1007/s10562-024-04808-6.

12. P. Bhanja, B. Mohanty, A. K. Patra, S. Ghosh, B. K. Jena, and A. Bhaumik, "IrO_2 and Pt Doped Mesoporous SnO_2 Nanospheres as Efficient Electrocatalysts for the Facile Oer and Her," *Chemcatchem* 11 (2019): 583–592, https://doi.org/10.1002/cctc.201801312.

13. W. He, L. Wang, H. Zhang, et al., "SnO_2@ MoS_2 Heterostructures Grown on Nickel Foam as Highly Efficient Bifunctional Electrocatalyst for Overall Water Splitting in Alkaline Media," *Journal of Alloys and Compounds* 938 (2023): 168678, https://doi.org/10.1016/j.jallcom.2022.168678.

14. K. B. Ibrahim, G. Darshan, G. Benetti, et al., "Enhanced Oxygen Evolution Reaction Performance of Niobium–Cobalt Oxide Catalysts in Acidic and Alkaline Media," *Advanced Sustainable Systems* 9 (2025): 2500385.

15. K. B. Ibrahim, T. Michelutti, A. Gradone, et al., "Electrochemically Modified $Mn_2P_4O_{12}$ as an Emerging Catalyst for Oxygen Evolution Reaction," *Advanced Materials Interfaces* 12 (2025): 2500216, https://doi.org/10.1002/admi.202500216.

16. Q. Zhao, Y. Zhang, C. Ke, X. Yang, and W. Xiao, "Anchoring a Pt-Based Alloy on Oxygen-Vacancy-Defected Mxene Nanosheets for Efficient Hydrogen Evolution Reaction and Oxygen Reduction Reaction," *Nanoscale* 15 (2023): 17516–17524, https://doi.org/10.1039/D3NR04071B.

17. N. Li, Y. Zhang, M. Jia, et al., "1t/2 h $MoSe_2$-on-Mxene Heterostructure as Bifunctional Electrocatalyst for Efficient Overall Water Splitting," *Electrochimica Acta* 326 (2019): 134976, https://doi.org/10.1016/j.electacta.2019.134976.

18. Y. Zhang, Z. Zhang, A. Addad, et al., "0D/2D Co_3O_4/Ti_3C_2 MXene Composite: A Dual-Functional Electrocatalyst for Energy-Saving Hydrogen Production and Urea Oxidation," *ACS Applied Energy Materials* 5 (2022): 15471–15482, https://doi.org/10.1021/acsaem.2c03052.

19. K. B. Ibrahim, K. Harrath, M. Hamrang, et al., "Ru-Doped Fe_2Tio_5 as a High-Performance Electrocatalyst for Urea-Assisted Water Splitting," *Small* 21 (2025): 2412370.

20. F. Lei, W. Liu, Y. Sun, et al., "Metallic Tin Quantum Sheets Confined in Graphene Toward High-Efficiency Carbon Dioxide Electroreduction," *Nature Communications* 7 (2016): 12697, https://doi.org/10.1038/ncomms12697.

21. M. Naguib, M. Kurtoglu, V. Presser, et al., "Two-Dimensional Nanocrystals Produced by Exfoliation of Ti_3AlC_2," in *Mxenes* (Jenny Stanford Publishing, 2023): 15–29, https://doi.org/10.1201/9781003306511.

22. P. Yan, R. Zhang, J. Jia, et al., "Enhanced Supercapacitive Performance of Delaminated Two-Dimensional Titanium Carbide/Carbon Nanotube Composites in Alkaline Electrolyte," *Journal of Power Sources* 284 (2015): 38–43, https://doi.org/10.1016/j.jpowsour.2015.03.017.

23. Z. Pan, F. Cao, X. Hu, and X. Ji, "A Facile Method for Synthesizing Cus Decorated Ti_3C_2 Mxene with Enhanced Performance for Asymmetric Supercapacitors," *Journal of Materials Chemistry A* 7 (2019): 8984–8992.

24. H. Wang, Y. Wu, J. Zhang, et al., "Enhancement of the Electrical Properties of Mxene Ti_3C_2 Nanosheets by Post-Treatments of Alkalization and Calcination," *Materials Letters* 160 (2015): 537–540, https://doi.org/10.1016/j.matlet.2015.08.046.

25. A. Iqbal and N. M. Hamdan, "Investigation and Optimization of Mxene Functionalized Mesoporous Titania Films as Efficient Photoelectrodes," *Materials* 14 (2021): 6292.

26. M. Chandran, A. Thomas, A. Raveendran, M. Vinoba, and M. Bhagiyalakshmi, "MoS_2 Confined Mxene Heterostructures as Electrode Material for Energy Storage Application," *Journal of Energy Storage* 30 (2020): 101446, https://doi.org/10.1016/j.est.2020.101446.

27. V. Natu, M. Benchakar, C. Canaff, A. Habrioux, S. Célérier, and M. W. Barsoum, "A Critical Analysis of the X-Ray Photoelectron Spectra of $Ti_3C_2T_z$ Mxenes," *Matter* 4 (2021): 1224–1251.

28. L. Kövér, Z. Kovács, R. Sanjinés, et al., "Electronic Structure of Tin Oxides: High-Resolution Study of Xps and Auger Spectra," *Surface and interface analysis* 23 (1995): 461–466.

29. D. Shuttleworth, "Preparation of Metal-Polymer Dispersions by Plasma Techniques. An Esca Investigation," *The Journal of Physical Chemistry* 84 (1980): 1629–1634, https://doi.org/10.1021/j100449a038.

30. C. Furlani, G. Mattogno, G. Polzonetti, R. Barbieri, E. Rivarola, and A. Silvestri, "Relationship Between Xps Core Binding Energies and Atomic Charge in Adducts of Sniv Derivatives With Pyrazine, and Comparison With Mössbauer Isomer Shift Data," *Inorganica Chimica Acta* 52 (1981): 23–28, https://doi.org/10.1016/S0020-1693(00)88566-7.

Supporting Information

Additional supporting information can be found online in the Supporting Information section.

Supporting File: admi70443-sup-0001-SuppMat.docx.